Letters

Preconditioned Iterative Solution of Scattering from Rough Surfaces

James C. West

***Abstract*—Extensions to the functionally identical forward–backward (FB) and method of ordered multiple interactions iterative techniques have recently been introduced that improve the convergence characteristics with specific scattering geometries. These extensions are shown to be mathematically equivalent to applying preconditioners to the discretized integral equation that is iteratively solved. The same preconditioners can be used with any iterative solution technique. Numerical examples show that the generalized minimal residual (GMRES) and bi-conjugate gradient–stable (BICGSTAB) algorithms give similarly rapid convergence when applied to a preconditioned discretized integral equation.**

***Index Terms*—Electromagnetic scattering by rough surfaces, iterative methods.**

I. Introduction

Recently, extensions have been introduced to the functionally identical forward–backward (FB) and method of ordered multiple interactions (MOMI) iterative approaches [both of which are particular implementations of the symmetric successive overrelaxation (SSOR) algorithm [1]] for rough surface scattering calculations that yield improved convergence properties for particular scattering geometries. Pino *et al.* [2] used an expanded self-interaction matrix with FB to give a procedure they termed the generalized FB technique that converged rapidly for a problem class where the original FB algorithm diverged. Adams and Brown [3] used a banded approximation of a factorized Helmholtz operator that increased the convergence speed of MOMI when applied to one-dimensionally rough single-valued surfaces. The convergence properties of other iterative algorithms can also be accelerated using these same approaches when applied to the same scattering problems.

II. Development

The discretized integral equation in rough-surface scattering calculations takes the form

$$\mathbf{Z}\mathbf{i} = \mathbf{v} \tag{1}$$

where $\mathbf{Z}$ is the interaction matrix (the discretized integral equation kernel), $\mathbf{i}$ is the unknown discretized surface current to be found, and $\mathbf{v}$ is the known discretized source vector. Iterative solution algorithms can be applied to (1) directly or can be applied to the preconditioned system [4]

$$\mathbf{M}^{-1}\mathbf{Z}\mathbf{i} = \mathbf{M}^{-1}\mathbf{v} \tag{2}$$

where $\mathbf{M}$ is the preconditioning matrix. $\mathbf{M}$ should be chosen both so that it approximates $\mathbf{Z}$ and so that $\mathbf{M}^{-1}\mathbf{x}$ is computationally inexpensive to solve, where $\mathbf{x}$ is any vector. Further refinement is achieved when the preconditioner is factored as $\mathbf{M} = \mathbf{M}_1\mathbf{M}_2$ and applied as

$$\mathbf{M}_1^{-1}\mathbf{Z}\mathbf{M}_2^{-1}[\mathbf{M}_2\mathbf{i}] = \mathbf{M}_1^{-1}\mathbf{v}. \tag{3}$$

The iterative procedure then solves for the vector $\mathbf{i}' = \mathbf{M}_2\mathbf{i}$ and the final solution is found from $\mathbf{i} = \mathbf{M}_2^{-1}\mathbf{i}'$. $\mathbf{M}_1$ and $\mathbf{M}_2$ are termed the left and right preconditioners, respectively.

The generalized self-interaction matrix defined by [2], designated $\mathbf{Z}^{sg}$, was introduced to allow FB to converge when there is an obstacle on or near the rough surface. It includes the diagonals of $\mathbf{Z}$ plus a block self-interaction submatrix corresponding to the obstacle under consideration. Multiplying (1) by the inverse of $\mathbf{Z}^{sg}$ gives

$$[\mathbf{Z}^{sg}]^{-1}\mathbf{Z}\mathbf{i} = [\mathbf{Z}^{sg}]^{-1}\mathbf{v}. \tag{4}$$

Some straightforward manipulations show that the generalized FB equations of [2, eq. (17), (18)] are obtained by applying the standard FB equations [their (8) and (9)] to (4) here. The generalized self-interaction matrix therefore acts as a preconditioner applied to the original linear system. $\mathbf{Z}^{sg}$ is, in fact, a block Jacobi preconditioner [4].

Adams and Brown [3] considered scattering from a randomly rough single-valued surface with Gaussian statistics. They first factored the interaction matrix as $\mathbf{Z} = \mathbf{C}_+\mathbf{C}_\pm\mathbf{C}_-$, where $\mathbf{C}_+$ and $\mathbf{C}_-$ are the lower and upper triangular submatrix components of $\mathbf{Z}$ (each including the diagonal elements), and introduced a banded approximation of $\mathbf{C}_\pm$ designated by $\tilde{\mathbf{C}}$. Letting $\mathbf{M}_1 = \mathbf{C}_+\tilde{\mathbf{C}}$ and $\mathbf{M}_2 = \mathbf{C}_-$, (3) becomes

$$\tilde{\mathbf{C}}^{-1}\mathbf{C}_\pm[\mathbf{C}_-\mathbf{i}] = \tilde{\mathbf{C}}^{-1}\mathbf{C}_+^{-1}\mathbf{v}. \tag{5}$$

Applying Richardson iteration (equivalent to a Neumann expansion [5]) to (5) gives (5) of Adams and Brown. The factorized Helmholtz-operation approach is, therefore, equivalent to applying Richardson iteration to (1) preconditioned by $\mathbf{M} = \mathbf{C}_+\tilde{\mathbf{C}}\mathbf{C}_-$.

Earlier, Donohue *et al.* [6] showed that the banded matrix interaction approximation (BMIA) approach for scattering from single-valued rough surfaces is equivalent to using a banded approximation of $\mathbf{Z}$ as a preconditioner with Richardson iteration.

III. Example

Preconditioners can be used with any iterative procedure. Here we consider two nonstationary algorithms as well as the stationary FB technique applied to the same scattering geometry used by Pino *et al.* [2] both with and without the preconditioning included in (1). (The term "stationary" indicates that the same iteration matrix is used to update the approximate solution on every iteration.) The nonstationary algorithms used are the generalized minimal residual (GMRES) and bi-conjugate gradient–stable (BICGSTAB) methods. Overviews of these algorithms are given in [4] and the particular implementations used here are described in [1]. For the preconditioned system of (2) these algorithms are formulated in terms of matrix–vector products (involving the original interaction matrix $\mathbf{Z}$) followed by the preconditioning step. Block–Jacobi preconditioning is performed by an initial single direct LU factoring of the preconditioner submatrix blocks followed by back-substitution during each iteration. The preconditioned nonstationary algorithms are, therefore, order $N^2 + M^3$, where N is the number of un-

Manuscript received July 20, 1999; revised March 14, 2000. This work was supported by the U.S. Office of Naval Research through the Sensing and Systems Division under Grant N00014-92-1206 and Grant N00014-96-1-0075 (program officer Dr. D. Trizna) and by the Ship Structures and Systems S&T Division (program officer Dr. R. P. Radlinski).

The author is with the School of Electrical and Computer Engineering, Oklahoma State University, Stillwater, OK 74078 USA.

Publisher Item Identifier S 0018-926X(00)05784-7.

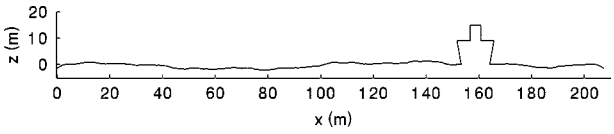

Fig. 1. Scattering geometry.

knowns in the complete system and M is the number of rows included in the blocks of the preconditioner, the same as the preconditioned FB technique. The residual vector of the original system that is used for the stopping test [1], [4] is recovered by multiplying the preconditioned residual vector by $\mathbf{Z}^{sg}$, an order M^2 step that does not add significant computational expense.

A test scattering configuration similar to that considered by Pino *et al.* [2] was generated, shown in Fig. 1. The ship structure used the same dimensions as that given by Pino *et al.* [2], and the surface to the left and right of the ship structure was realized from the Pierson–Moskowitz wave-height spectrum assuming a 15 m/s wind speed. The magnetic field integral equation (MFIE) for describing vertical polarization scattering from a perfectly conducting interface was discretized using the same hybrid moment-method/geometrical theory of diffraction approach used in [1]. Plane wave illumination from the left at a grazing angle of 10° and a wavelength of 1 m was assumed. A sampling of 20 pulse basis functions per wavelength was used, giving 2416 unknowns.

The resulting linear system was first treated using the FB, GMRES, and BICGSTAB algorithms without preconditioning (i.e., (1) was directly solved). The convergence histories of the normalized residual error ($R_N = \|\mathbf{v} - \mathbf{Z}\mathbf{i}^{(n)}\|/\|\mathbf{v}\|$, where $\mathbf{i}^{(n)}$ is the approximate solution after the nth iteration) are shown in Fig. 2. The residuals are plotted versus the equivalent number of matrix–vector (MV) multiply operations needed both to perform the iteration and to calculate the normalized residual needed to perform a valid stopping test (1.5, 2, and 1 per iteration for FB, BICSTAB, and GMRES, respectively) [1], and the restart period of GMRES was set sufficiently small (75) with respect to number of unknowns so that the per-iteration overhead was small compared to the MV operation time. The discretized MFIE used here yields interaction matrices that are naturally better conditioned than that obtained from the EFIE used by Pino *et al.* [2], so FB is slowly convergent but needs 350 MV's to reach a normalized residual of 10^{-3}. BICGSTAB convergence is more rapid but quite ragged, reaching the same residual after 82 MV's. GMRES is both faster and smoother than BICGSTAB, reaching $R_N = 10^{-3}$ after 53 MV's.

The convergence histories of the algorithms when applied with the preconditioning are shown in Fig. 3. As in [2], the generalized self-interaction block included the matrix elements corresponding to the ship itself as well as short segments of the sea surface extending 5 m beyond the left and right limits of the ship. The preconditioned (generalized) FB technique shows the fastest convergence, needing only 6 MV's to reach $R_N = 10^{-3}$. This is followed by GMRES, which reaches the same level after 10 MV's and then BICGSTAB, which requires 12 MV s.

IV. Comments

As seen, both stationary and nonstationary iterative algorithms can benefit from the use of a carefully chosen preconditioner. Other preconditioners that are available that may prove useful with other scattering problems are summarized in [4]. There are tradeoffs that must be considered when selecting the underlying technique to be used for a particular problem. The nonstationary approaches have the advantage that their convergence properties are much less sensitive to the conditioning of the system ultimately achieved (after preconditioning) [1].

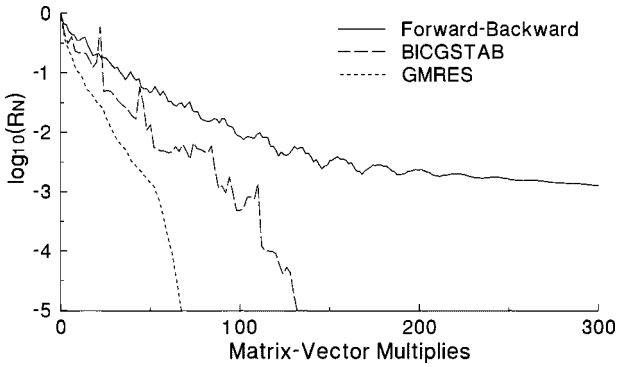

Fig. 2. Convergence of iterative techniques with no preconditioning.

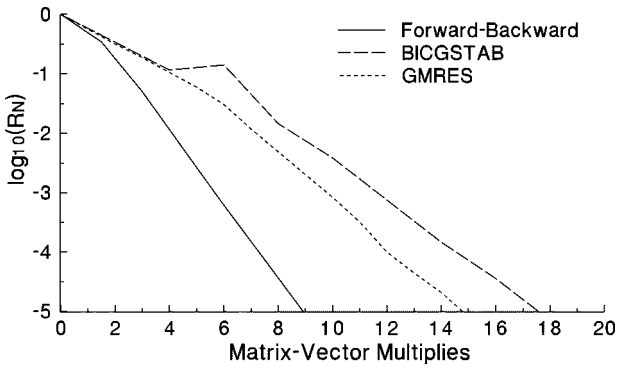

Fig. 3. Convergence of iterative techniques with block Jacobi preconditioning.

This is desirable in cases where it is not cost effective to tailor a preconditioner to every specific problem, or the cost of evaluating the preconditioner is large compared to the cost of an iteration (for example, if the size of an obstacle is such that M^3 is large compared to N^2). Also, block Jacobi preconditioning combined with nonstationary iterative routines are particularly well suited to parallel processing, where the true matrix–vector multiplications can be performed much more efficiently than the FB-substitution operations of FB [4]. On the other hand, as shown here, the stationary FB or MOMI converges in fewer MV operations (sometimes as little as one half) when very good conditioning is achieved. This can be important if performing the iterations themselves is particularly expensive (such as when the interaction matrix elements must be regenerated each time they are used).

References

[1] J. C. West and J. M. Sturm, "On iterative approaches for electromagnetic rough-surface scattering problems," *IEEE Trans. Antennas Propagat.*, vol. 47, pp. 1281–1288, Aug. 1999.

[2] M. R. Pino, L. Landesa, J. L. Rodríguez, F. Obelleiro, and R. J. Burholder, "The generalized forward-backward method for analyzing the scattering from targets on ocean-like rough surfaces," *IEEE Trans. Antennas Propagat.*, vol. 47, pp. 961–969, June 1999.

[3] R. J. Adams and G. S. Brown, "An iterative solution of two-dimensional rough surface scattering problems based on a factorization of the helmholtz operator," *IEEE Trans. Antennas Propagat.*, vol. 47, pp. 765–766, Apr. 1999.

[4] R. Barrett, M. Berry, T. F. Chan, J. Demmel, J. Donato, J. Dongarra, V. Eijkhout, R. Poza, C. Romine, and H. B. der Vort, *Templates for the Solution of Linear Systems: Building Blocks for Iterative Methods*. Philadelphia, PA: SIAM, 1994.

[5] D. M. Young and T.-Z. Mai, "The search for omega," in *Iterative Methods for Large Linear Systems*, D. R. Kincaid and L. J. Hayes, Eds. New York: Academic, 1990, pp. 293–311.

[6] D. J. Donohue, H.-C. Ku, and D. R. Thompson, "Application of iterative moment-method solutions to ocean surface radar scattering," *IEEE Trans. Antennas Propagat.*, vol. 46, pp. 121–132, Jan. 1998.

An MFIE-Based Tabulated Interaction Method for UHF Terrain Propagation Problems

Conor Brennan, Peter J. Cullen, and Luca Rossi

***Abstract*—Approximations are introduced into a magnetic field integral equation (MFIE) formulation of a two-dimensional (2-D) terrain scattering problem, which allow most of the integrals inherent in the MFIE to be performed analytically. The implementation of the method is discussed and an example is given comparing its performance against a reference solution and measured data. The new formulation applies to both TM^z and TE^z polarizations and is an improvement over the electric field integral equation (EFIE) formulation of the tabulated interaction method (TIM) in that far-field patterns can be calculated analytically leading to increased flexibility of the method.**

***Index Terms*—Integral equation methods, UHF radio propagation.**

I. Formulation

Referring to Fig. 1 we note that our terrain profile is modeled as a series of connected perfectly electrically conducting linear segments. The central point of segment G_L will be denoted by the vector $\boldsymbol{\rho}_l$. Assuming time harmonic variations of the form $\exp(j\omega t)$ we can write the MFIE for the current at point $\boldsymbol{\rho}_i \in G_L$ in the case of TM^z polarization (though the analysis for TE^z is similar) as

$$J_z(\boldsymbol{\rho}_i) = K_z(\boldsymbol{\rho}_i) - \frac{\beta_J}{2} \sum_{L' \neq L} \int_{\boldsymbol{\rho}_j \in G_{L'}} \mathcal{G}_{ij} J_z(\boldsymbol{\rho}_j)\, dc \tag{1}$$

where $\boldsymbol{J} \equiv J_z\hat{\boldsymbol{z}}, \boldsymbol{K} \equiv K_z\hat{\boldsymbol{z}}$ and

$$\boldsymbol{K}(\boldsymbol{\rho}_i) = 2\hat{\boldsymbol{n}}(\boldsymbol{\rho}_i) \times \boldsymbol{H}^{\mathrm{inc}}(\boldsymbol{\rho}_i) \tag{2}$$

$$\mathcal{G}_{ij} = H_1^{(2)}(\beta|\boldsymbol{\rho}_i - \boldsymbol{\rho}_j|)\hat{\boldsymbol{n}}(\boldsymbol{\rho}_i) \cdot \boldsymbol{\rho}_{ji} \tag{3}$$

where $\boldsymbol{\rho}_{ji} = \boldsymbol{\rho}_i - \boldsymbol{\rho}_j$ and $\beta = 2\pi/\lambda$ is the wavenumber of the radiation of wavelength λ.

We propose introducing two approximations which will allow the majority of the integrals occurring in equation (1) to be calculated analytically. This is in contrast to standard moment-method-based solutions, which are effectively forced to calculate such integrals numerically, a requirement that leads to their well-documented computational burden. The approximations are

$$K_z(\boldsymbol{\rho}_i) \simeq K_z(\boldsymbol{\rho}_l) \exp(j\beta\hat{\boldsymbol{\rho}}_{la} \cdot \boldsymbol{\rho}_{li}) \tag{4}$$

$$\int_{G_{L'}} \mathcal{G}_{ij} J_z(\boldsymbol{\rho}_j)\, dc \simeq \mathcal{G}_{ll'} \exp(j\beta\hat{\boldsymbol{\rho}}_{ll'} \cdot \boldsymbol{\rho}_{li}) \mathcal{F}^{L'}(\hat{\boldsymbol{\rho}}_{l'l}) \tag{5}$$

where (5) is derived using the fast far-field approximation (FAFFA) [1] and

$$\mathcal{F}^{L'}(\hat{\boldsymbol{\rho}}_{l'l}) = \frac{\beta_J}{2} \int_{G_{L'}} J_z(\boldsymbol{\rho}_j) \exp(j\beta\hat{\boldsymbol{\rho}}_{l'l} \cdot \boldsymbol{\rho}_{l'j})\, dc. \tag{6}$$

Manuscript received December 15, 1998; revised December 16, 1999.

The authors are with the Department of Electrical Engineering, Trinity College, Dublin 2, Ireland.

Publisher Item Identifier S 0018-926X(00)05782-3.

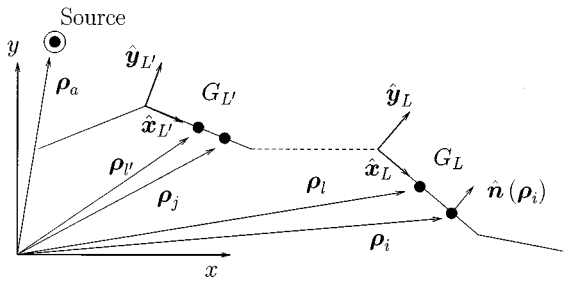

Fig. 1. Geometry for terrain propagation problem. Note that terrain profile consists of large linear segments G_L each with a central point $\boldsymbol{\rho}_l$. The source is located at $\boldsymbol{\rho}_a$. Broken line indicates intervening terrain profile.

To proceed, we define a segment's far-field pattern; that is $\mathcal{F}_q^{L'} \equiv \mathcal{F}^{L'}(\hat{\boldsymbol{e}}_{L'}(\theta_q))$ for the unit vectors $\hat{\boldsymbol{e}}_{L'}(\theta_q)$ with $q = 1 \cdots Q$ and $\theta_q = q\Delta\theta$ where $\Delta\theta = 2\pi/Q$. The unit vectors are defined by

$$\hat{\boldsymbol{e}}_{L'}(\phi) = \hat{\boldsymbol{x}}_{L'} \cos\phi + \hat{\boldsymbol{y}}_{L'} \sin\phi \tag{7}$$

where $\hat{\boldsymbol{x}}_{L'}$ and $\hat{\boldsymbol{y}}_{L'}$ define a coordinate system relative to segment $G_{L'}$ as depicted in Fig. 1. If $\Delta\theta$ is small enough we can interpolate between the far-field pattern values to give a solution to $\mathcal{F}^{L'}(\hat{\boldsymbol{\rho}}_{l'l})$ for any particular direction $\hat{\boldsymbol{\rho}}_{l'l}$ that may arise. Our aim thus becomes the analytical evaluation of a segment's far-field pattern.

Inserting (4) and (5) into (1) forces the the current to take a very specific form over each segment.

Specifically, we can write the current residing on segment G_L in a simple form as

$$J_z(\boldsymbol{\rho}_i) \simeq \sum_{q=1}^{Q} A_q^L \exp(j\beta\hat{\boldsymbol{e}}_L(\theta_q) \cdot \boldsymbol{\rho}_{li}) \tag{8}$$

where

$$A_q^L = \psi_q(\phi_{la}) K_l - \sum_{L' \neq L} \psi_q(\phi_{ll'}) \mathcal{G}_{l'l} \mathcal{F}^{L'}(\hat{\boldsymbol{\rho}}_{l'l}) \tag{9}$$

where (see Fig. 1) ϕ_{la} ($\phi_{ll'}$) is the angle that the vector $\boldsymbol{\rho}_{la}$ ($\boldsymbol{\rho}_{ll'}$) makes with $\hat{\boldsymbol{x}}_L$. The interpolating factors ψ are given by

$$\psi_q(\zeta) = \frac{|\zeta - \theta_{q-1}|}{\Delta\theta} \quad \text{for } \theta_{q-1} < \zeta < \theta_q \tag{10}$$

$$= \frac{|\zeta - \theta_{q+1}|}{\Delta\theta} \quad \text{for } \theta_q < \zeta < \theta_{q+1} \tag{11}$$

$$= 0 \text{ otherwise.} \tag{12}$$

This allows us to write, inserting (8) into (6) and recalling the definition of a segment's far-field pattern

$$\mathcal{F}_r^L = \sum_{q=1}^{Q} \int_{G_L} A_q^L \exp(j\beta\boldsymbol{f}_L(q,r) \cdot \boldsymbol{\rho}_{li})\, dc \tag{13}$$

where

$$\boldsymbol{f}_L(q,r) = \hat{\boldsymbol{e}}_L(\theta_q) + \hat{\boldsymbol{e}}_L(\theta_r). \tag{14}$$

It is easy to show that, as $\hat{\boldsymbol{\rho}}_{li} = \pm\hat{\boldsymbol{x}}_L$

$$\mathcal{F}_r^L = \sum_{q=1}^{Q} A_q^L \int_{-a/2}^{a/2} \exp(\jmath s\beta f(q,r))\, ds \tag{15}$$

$$= \sum_{q=1}^{Q} A_q^L I(q,r,a) \tag{16}$$

where $f(q,r) = \cos\theta_q + \cos\theta_r$, a is the arclength of the segment and

$$I(q,r,a) = \begin{cases} a, & f(q,r) = 0 \\ 2\sin(a\beta f(q,r)/2)/\beta f(q,r), & \text{otherwise.} \end{cases} \tag{17}$$

Solving the problem reduces to calculating the coefficients A_q^L. Equations (9) and (16) together can be taken to define a matrix equation for the A_q^L. This governing matrix is sparse and can be solved by a number of different iterative schemes though this is beyond the scope of this communication. A simple solution is to truncate the summation of (9) at $L-1$, thereby assuming forward scattering and allowing for the sequential calculation of the A_q^L coefficients. Once known, these coefficients are used via (16) to trivially calculate the far-field pattern for that segment, which in turn is used in the calculation of the coefficients associated with subsequent segments as well as the electric field above the surface. It is important to note that, considering the geometry of typical terrain problems, which leads to near-grazing propagation, the majority of the coefficients A_q^L will equal zero. Only coefficients pertaining to propagation in the near-horizontal direction will be excited. Hence, our current description is very much compressed, a few A_q^L coefficients is all that is necessary to describe a current residing on a group. In the numerical example presented in Section II the maximum number of coefficients needed to represent the current on any segment was 13. This is in contrast to a standard pulse-basis approach, which would have required over 300 unknowns per segment. This compression means that far-field patterns can be calculated very efficiently indeed and the complexity of the method reduces to $O(M^2)$ where M is the number of segments used in the problem.

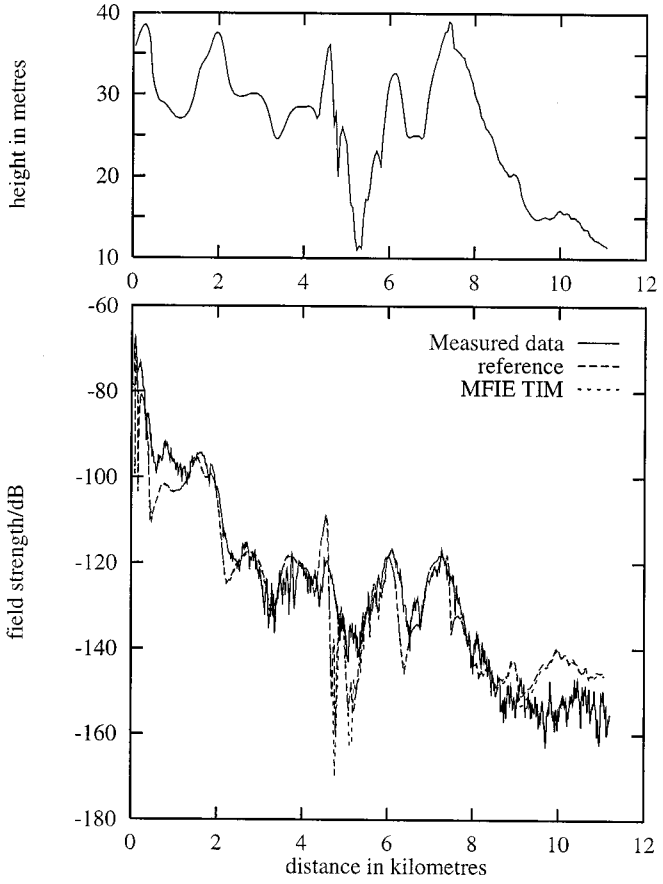

Fig. 2. Fields (bottom) 2.4 m over terrain profile (top) at 970 MHz. Source situated at (0.0,45.4). 100 m of terrain added from (0.0,35.0) to (−100.0, 35.0) as buffer to prevent spurious diffraction due to nonclosed nature of problem. Terrain was sampled at 50 m intervals and we worked with linear segments 25 m in length. FAFFA was used to explicitly compute current samples and far-field patterns for first 150 m of profile. Analytic far-field patterns were used for the rest of the terrain. $\Delta\theta = \pi/200$ and in order to calculate near-field interactions we used $P = 30$ subsegments. The near-field was restricted to the interaction between adjoining segments.

II. Implementational Issues and Numerical Results

First, one should note that in cases where each segment is the same length a, the quantities $I(q,r,a)$, being the essential "building blocks" of each segment's far-field pattern as per (16), will be required repeatedly throughout the implementation. To ensure efficiency they should be calculated once for each pair (q,r) and stored in a matrix to be used as required. Our previous formulation [2] was based on an EFIE and did not allow a simple analytic formula for $I(q,r)$ such as is given by (17). Instead these important quantities were numerically tabulated and imported from problem to problem. Subsequent work [3] has suggested that such approximate analytical results are possible within the EFIE framework though they are more complicated than the simple results presented here.

In addition, when one considers the geometries of typical terrain profiles it is understood that we only need calculate and store group far-field patterns for a limited range of near-grazing angles. Hence, we need only calculate the "building blocks" $I(q,r)$ for pairs (q,r) relating to propagation residing within a few degrees of grazing. The memory requirements of the TIM are thus of a similar order to the FAFFA.

The second issue is that the introduction of the approximation (4) is invalid in the immediate vicinity of the source, rendering (8) and the subsequent analytical evaluation of the far-field patterns invalid for segments in this region. This problem is easily rectified by explicitly calculating current samples in this region using the fast far-field algorithm [1] or some other such fast scheme and numerically calculating the far-field patterns of these near-source segments.

The final issue is that the geometric approximations underpinning (5) become less accurate as the "scattering" segment $G_{L'}$ approaches the "receiving" segment G_L. In the case of such near-neighbor interactions the authors found it useful to subdivide segment $G_{L'}$ into P subsegments $G_{L'}^p$, for $p = 1 \cdots P$, each with center $\boldsymbol{\rho}_p$. We can define the far-field pattern $\mathcal{F}_r^{L'(p)}$ of each of the P subsegments, thus

$$\mathcal{F}_r^{L'(p)} = \sum_{q=1}^{Q} A_q^{L'} \exp(\jmath\beta\hat{\boldsymbol{e}}_{L'}(\theta_q)\cdot\boldsymbol{\rho}_{l'p}) I(q,r,a/P) \tag{18}$$

where each subsegment is now of arclength a/P. We then use the more precise relation

$$\int_{G_{L'}} \mathcal{G}_{ij} J_z(\boldsymbol{\rho}_j)\, dc \simeq \sum_{p=1}^{P} \mathcal{G}_{lp} \exp(j\beta \hat{\boldsymbol{\rho}}_{lp} \cdot \boldsymbol{\rho}_{li}) \mathcal{F}^{L'(p)}(\hat{\boldsymbol{\rho}}_{pl}) \tag{19}$$

where $\mathcal{F}^{L'(p)}(\hat{\boldsymbol{\rho}}_{pl})$ can be found by interpolating between the $\mathcal{F}_r^{L'(p)}$.

The computational technique outlined in this paper has been used to calculate fields over several terrain profiles for which experimental data has been made available. Fig. 2 illustrates the excellent agreement between the fields predicted by the techniques outlined in this paper and both the measured data and a slow reference solution which used a forward scattering EFIE-based solution. Our new computational method, running on an IBM Power PC, took 5 s to give the results shown. This should be compared with computation times of the order of a day for the reference solution. Our experience has shown that most practical terrain propagation problems can be accurately analyzed using the TIM. However, the geometrical approximations underpinning the method become suspect when applied to structures with sharp wedge-like protusions such as buildings etc. In these cases it is advisable to consider a hybrid FAFFA/tabulated interaction method (TIM) approach allowing for more accurate near-field analysis in problem areas as required. In conclusion, the ability to analytically describe the currents residing on a given segment and, hence, its far-field pattern lends a great flexibility to our new MFIE-based formulation of the TIM.

ACKNOWLEDGMENT

The authors would like to thank Forbairt, Ireland for supporting this research and Prof. B. Andersen, Aalborg University, Denmark, for supplying the terrain profile and measurements used in this communication.

REFERENCES

[1] C. C. Lu and W. C. Chew, "Fast far-field approximation for calculating the RCS of large objects," *Microwave Opt. Tech. Lett.*, vol. 8, no. 5, pp. 238–241, 1995.

[2] C. Brennan and P. J. Cullen, "Tabulated interaction method for UHF terrain propagation problems," *IEEE Trans. Antennas Propagat.*, vol. 46, pp. 738–740, May 1998.

[3] L. Rossi, P. J. Cullen, and C. Brennan, An analytical approximation of the TIM look-up table, in COST259 TD(99) Meet., Jan. 1999.

Analysis of Aperture-Coupled Hemispherical Dielectric Resonator Antenna with a Perpendicular Feed

K. W. Leung

***Abstract*—The aperture-coupled dielectric resonator antenna (DRA) with a perpendicular feed is studied theoretically and experimentally. This excitation scheme has the advantage that it isolates the DRA from active circuitry and meanwhile fully utilizes the whole feed substrate for active-circuitry integration. The effects of the slot length, slot offset, and substrate permittivity on the input impedance are discussed.**

***Index Terms*—Dielectric resonator antennas.**

I. INTRODUCTION

The dielectric resonator antenna (DRA) [1] is an attractive radiator because of having no metallic loss. It offers other advantages such as small size, light weight, low cost, and ease of excitation. Moreover, the DRA can be easily integrated with active circuitry and a number of excitation schemes [2]–[7] were investigated for this purpose. In these excitation schemes the DRA resides either on the feedline side or on the ground plane side. The former suffers from the problem of spurious coupling between the DRA and active circuitry, whereas in the latter the DRA occupies one side of the feed substrate and, thus, substantially reduces the usable substrate area. To solve these problems, the aperture-coupled DRA with a perpendicular feed has been proposed recently [8]. This method is especially useful for implementation of large phased arrays where a large substrate area is required to accommodate phase shifters, amplifiers, feed lines, bias lines, etc. Thus far, the study has been solely experimental and limited to the cylindrical DRA only. In this letter, the hemispherical DRA version is studied theoretically and experimentally, with the DRA excited at the fundamental TE_{111} mode [5], [9]. The effects of the slot length and offset on the input impedance are discussed. Moreover, the effect of substrate permittivity, which has not been investigated in [8] is also reported in this letter.

II. THEORY

The geometry of the antenna configuration is shown in Fig. 1, where a hemispherical DRA of radius a and dielectric constant ε_{ra} is excited by a slot of length L and width W. In general the DRA has offsets y_d and z_d from the z-axis and y-axis, respectively. A 50-Ω microstripline of width W_f is printed on the perpendicular feed substrate of dielectric constant ε_{rs} and thickness d. The cross section of the substrate was used to feed the slot. At the aperture position, the mircrostripline and its ground plane are electrically connected to the DRA ground plane.

The approach of [10] is used in the analysis. By using the equivalence principle, the slot is short-circuited and the fields are generated by two equivalent magnetic currents flowing on adjacent sides of the DRA ground plane. First consider the feedline part. The microstripline is assumed to be propagating a quasi-TEM mode of fields $\vec{E}^{\pm} = \vec{e} e^{\mp j\beta_f x}$ and $\vec{H}^{\pm} = \pm \vec{h} e^{\mp j\beta_f x}$, where $\vec{e}(y,z) = e_y \hat{y} + e_z \hat{z}$ and $\vec{h}(y,z) = h_y \hat{y} + h_z \hat{z}$ are normalized transverse modal fields [11] and β_f is the propagation constant of the microstripline fields. Suppose there is an incident signal of fields $\vec{E}^{+}, \vec{H}^{+}$, which propagates from the input microstripline port. Then the reflected signal from the

Manuscript received September 25, 1998; revised March 27, 2000. This work was supported by the RGC Research Grant 9040209.

The author is with the Department of Electronic Engineering, City University of Hong Kong, Kowloon, Hong Kong.

Publisher Item Identifier S 0018-926X(00)05781-1.

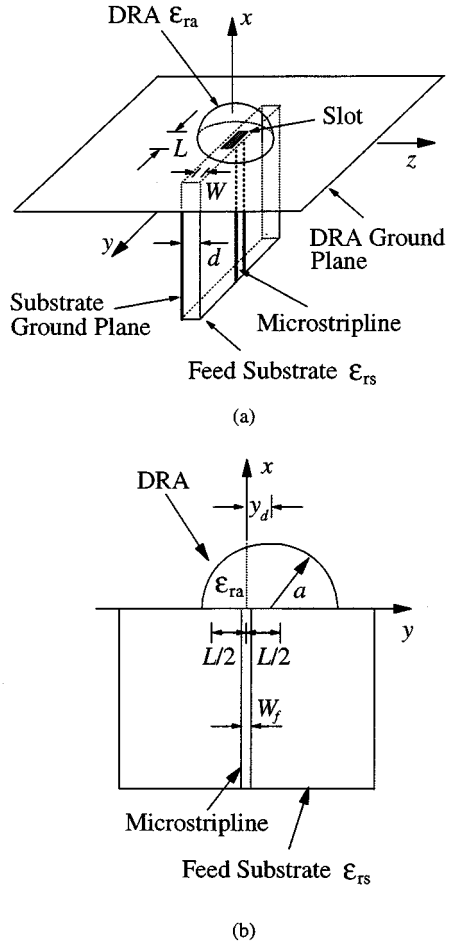

Fig. 1. The geometry of the aperture-coupled hemispherical DRA with a perpendicular feed. (a) Perspective view. (b) Front view.

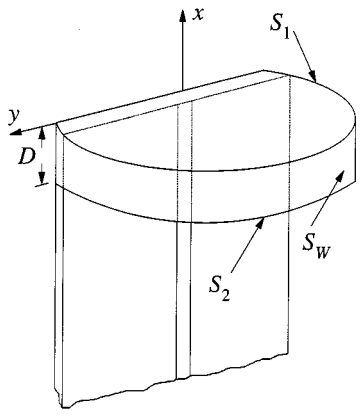

Fig. 2. Illustration of the surfaces S_1, S_2, and S_W used in the reciprocity analysis.

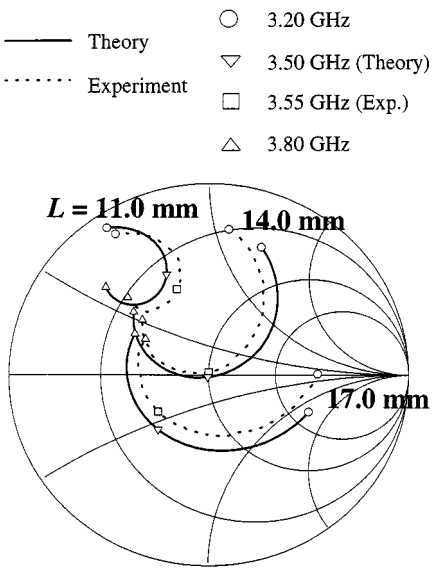

Fig. 3. Measured and calculated input impedance of the DRA for $L = 11.0, 14.0$, and 17.0 mm: $a = 12.5$ mm, $\varepsilon_{ra} = 9.5$, $W = 0.9$ mm, $\varepsilon_{rs} = 2.33, d = 1.57$ mm, and $W_f = 4.6$ mm.

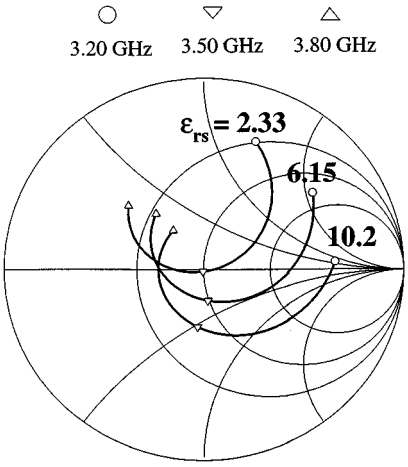

Fig. 4. Calculated input impedance of the DRA for $\varepsilon_{rs} = 2.33, 6.15$, and 10.2: $a = 12.5$ mm, $\varepsilon_{ra} = 9.5$, $L = 14.0$ mm, $W = 0.9$ mm, and $d = 1.57$ mm.

DRA ground plane consists of two parts; part A is a total reflection caused by the short-circuited slot and part B the fields excited by the equivalent magnetic current M_y on the substrate side. The total fields in part A are given by $\vec{E}_A = \vec{E}^+ + R_A\vec{E}^-$, $\vec{H}_A = \vec{H}^+ + R_A\vec{H}^-$ and in part B by $\vec{E}_B = R_B\vec{E}^-$, $\vec{H}_B = R_B\vec{H}^-$, where $R_A = -1$ is the reflection coefficient of the short-circuited slot and R_B is the excitation coefficient of the magnetic current. The total refection coefficient of the incident signal is then given by $R = R_A + R_B = R_B - 1$. To determine R_B, the reciprocity theorem is applied to $\vec{E}_A, \vec{H}_A$ and $\vec{E}_B, \vec{H}_B$ as follows:

$$\iint_S \vec{E}_A \times \vec{H}_B \cdot d\vec{S} = \iint_S \vec{E}_B \times \vec{H}_A \cdot d\vec{S} \tag{1}$$

where S is a closed surface consisting of three pieces, namely S_1, S_2, and S_W. The surface S_1 coincides with the DRA ground plane, whereas S_2 is parallel to and displaced from S_1, as shown in Fig. 2. The distance D between the surfaces is arbitrary, as their terms are cancelled out each other during the formulation. S_W is a side wall which connects S_1 and S_2. It was found that the contributions of S_W to the integrals were zero. On S_1, we have $\vec{E}_A = 0$ but

$\hat{n} \times \vec{E}_B = M_y \hat{y}$ on the original slot surface S_0. Using these facts (1) is reduced to:

$$R_B = \iint_{S_0} M_y(y,z) h_y(y,z)\, dS \tag{2}$$

which is the result of [10].

The next step is to enforce the continuity of tangential H-fields across the slot, resulting in an integral equation for the magnetic current M_y. In addition to (2), we have two equations for the two unknowns R_B and M_y. Use is made of the moment method to expand the magnetic current M_y as $M_y(y,z) = \Sigma_{n=1}^{N} V_n f_u(z) f_p(y - y_n)$, where $f_u(z)$ and $f_p(y)$ are pulse and piecewise sinusoidal (PWS) functions [5], respectively. Employing the Galerkin's procedure, two matrix equations that correspond to the integral equation and to $R = R_B - 1$ are obtained, from which the unknown voltage matrix is solved

$$[V_n] = \{[Y_{mn}^a - Y_{mn}^s] + [\Delta v_m][\Delta v_n]^t\}^{-1}[2\Delta v_m] \tag{3}$$

where Y_{mn}^a and Y_{mn}^s are DRA and substrate admittances, respectively, and Δv_m is associated with the feedline field. The superscript t denotes the transpose of a matrix. Evaluation of Y_{mn}^a is performed in the same manner as before [5]. However, this is not the case for Y_{mn}^s and Δv_m because the slot is now on the cross section of the substrate, not on the substrate ground plane. Evaluation of Y_{mn}^s and Δv_m thus involves integrations of z, which are performed analytically in spatial domain. On the other hand, the integrations of y are performed, as usual, in spectral domain. Finally, the reflection coefficient is given by $R = [\Delta v_m]^t[V_n] - 1$ from which the input impedance at the slot position is easily found through $Z_{\text{in}} = (1 + R)/(1 - R)$.

III. Results

A hemispherical DRA of radius $a = 12.5$ mm and dielectric constant $\varepsilon_{ra} = 9.5$ was measured using an HP8510C network analyzer. To avoid the air-gap error [12], conducting adhesive tapes were mounted on a foam board to form the DRA ground plane. The DRA was placed on the adhesive side of the conducting tapes to remove any possible air gap between itself and the ground plane. Although an effective air gap due to the adhesive material may exist, the effect is much smaller than for an air-filled gap. Fig. 3 shows the measured and calculated input impedances for $L = 11.0, 14.0,$ and 17.0 mm, with the slot located at the center of the DRA (i.e., $y_d = z_d = 0$). Reasonable agreement between theory and experiment is obtained. It is observed that the coupling (radius of impedance circle [5]) increases with L, as expected. An excellent impedance match is obtained for $L = 14$ mm, at which the measured and calculated resonant frequencies (min $|S_{11}|$) are 3.55 and 3.50 GHz (error 1.4%), respectively. The frequencies are very close to the predicted value given in [5].

Fig. 4 shows the calculated input impedance for different substrate permittivities with $L = 14.0$ mm and $y_d = z_d = 0$. In each case, the width of the microstripline is changed to maintain a 50-Ω feedline. With reference to the figure, using a higher ε_{rs} results in a stronger coupling. This is because increasing ε_{rs} will decrease the effective wavelength in the slot and, thus, lengthens the slot electrically. The effects of the slot offsets y_d and z_d on the input impedance were also studied. It was found that the results, like the effect of the slot length, were very similar to those of the previous configuration [5] and are omitted here for brevity.

References

[1] S. A. Long, M. W. McAllister, and L. C. Shen, "The resonant cylindrical dielectric cavity antenna," *IEEE Trans. Antennas Propagat.*, vol. AP-31, pp. 406–412, May 1983.

[2] R. A. Kranenburg and S. A. Long, "Microstrip transmission line excitation of dielectric resonator antennas," *Electron. Lett.*, vol. 24, pp. 1156–1157, Sept. 1988.

[3] R. A. Kranenburg, S. A. Long, and J. T. Williams, "Coplanar waveguide excitation of dielectric resonator antennas," *IEEE Trans. Antennas Propagat.*, vol. 39, pp. 119–122, Jan. 1991.

[4] J. T. H. St. Martin, Y. M. M. Antar, A. A. Kishk, and A. Ittipiboon, "Dielectric resonator antenna using aperture coupling," *Electron. Lett.*, vol. 26, pp. 2015–2016, Nov. 1990.

[5] K. W. Leung, K. M. Luk, K. Y. A. Lai, and D. Lin, "Theory and experiment of an aperture-coupled hemispherical dielectric resonator antenna," *IEEE Trans. Antennas Propagat.*, vol. 43, pp. 1192–1198, Nov. 1995.

[6] G. P. Junker, A. A. Kishk, and A. W. Glisson, "Input impedance of aperture coupled dielectric resonator antenna," *IEEE Trans. Antennas Propagat.*, vol. 44, pp. 600–607, May 1996.

[7] G. P. Junker, A. A. Kishk, A. W. Glisson, and J. Guo, "Input impedance of microstrip-slop-coupled dielectric resonator antennas mounted on thin dielectric layers," *Microwave Millimeter-Wave Comput.-Aided Eng.*, vol. 6, pp. 174–182, 1996.

[8] K. W. Leung and M. W. To, "Aperture-coupled dielectric resonator antenna with a perpendicular feed," *Electron. Lett.*, vol. 33, pp. 1000–1001, June 1997.

[9] A. A. Kishk, G. Zhou, and A. W. Glisson, "Analysis of dielectric resonator antennas with emphasis on hemispherical structures," *IEEE Antennas Propagat. Mag.*, vol. 36, pp. 20–31, Apr. 1994.

[10] N. K. Das, "Rigorous analysis of an aperture-coupled microstrip antenna fed by a microstrip line on a perpendicular substrate," *IEEE Microwave Guided Wave Lett.*, vol. 4, pp. 202–204, June 1994.

[11] D. M. Pozar, "A reciprocity method of analysis for printed slot and slot-coupled microstrip antennas," *IEEE Trans. Antennas Propagat.*, vol. AP-34, pp. 1439–1446, Dec. 1986.

[12] G. P. Junker, A. A. Kishk, A. W. Glisson, and D. Kajfez, "Effect of air gap on cylindrical dielectric resonator antenna operating in TM_{01} mode," *Electron. Lett.*, vol. 30, pp. 97–98, Jan. 1994.

Traveling-Wave Analysis of a Bifilar Scanning Helical Antenna

Robert K. Zimmerman, Jr.

***Abstract*—The bifilar scanning helical antenna is analyzed by considering the structure to carry a single traveling wave. It is shown that the relative phase velocity (v/c) must equal unity to yield the scanning features shown by numerical experiment. This is at complete odds with monofilament helices (Kraus), which display a slow wave structure.**

***Index Terms*—Helical antenna, scanning antennas.**

I. Introduction

Nakano *et al.* [1] were the first to document the scanning feature of bifilar helical antennas with large pitch angles. In their paper, they numerically analyzed the radiation pattern from a bifilar helix, as shown in Fig. 1. The helix diameter was about 0.08λ with a pitch angle a of 68°. A six turn helix, with a 400 Ω resistive

Manuscript received September 13, 1998; revised March 6, 2000.

The author is with Lawrence Behr Associates, Inc., Greenville, NC 27835 USA.

Publisher Item Identifier S 0018-926X(00)05780-X.

load at the end, was used to emulate a longer structure. The resistive load terminates the traveling-wave structure so that the effects due to reflected waves are minimized—as if the antenna were much longer. Nakano documented a major conical radiation lobe that scanned in direction (from backfire to normal) over the frequency range 1.3–2.5 GHz. This is shown in Figs. 2 and 3. In the following section, we analyze the structure to show that this feature is due to wave propagation on the helix with $v/c = 1$.

II. Analysis

The following analysis will use the helix presented in crossview in Fig. 4. The notation below will be used:

D	diameter of helix (center to center);
S	spacing between turns (center to center);
α	pitch angle = arctan$(S/\pi D)$;
L	length of one turn;
n	number of turns;
A	axial length = nS;
ϕ	direction of major radiation lobe;
θ	$180^\circ - \phi$;
p	relative phase velocity $= v/c$.

Consider the condition for the wavefront shown to exist: we must have the phase delay over path A plus the phase length over the path Q sum to an integral number of wavelengths. If the wave traveling up the helix has relative phase velocity $p = v/c$, the total phase length over path A (n turns) is

$$(nL/p\lambda) = n(\pi D/\cos\alpha)/p\lambda$$

as can be seen with the aid of Fig. 5 showing a turn of the helix "unwound."

The phase length for path Q is

$$Q/\lambda = (A\cos\phi)/\lambda = nS(\cos\phi)/\lambda = [n(\pi D\tan\alpha)\cos\phi]/\lambda.$$

Accordingly, for closure we must have

$$n(\pi D/\cos\alpha)/p\lambda + [n(\pi D\tan\alpha)\cos\phi]/\lambda = m$$

where m is an integral number of wavelengths. For a first-order lobe $n = m$ and we have

$$1/(p\cos\alpha) + (\tan\alpha)(\cos\phi) = \lambda/\pi D$$

which may be immediately solved for ϕ

$$\phi = \arccos\left\{\frac{1}{\tan\alpha}\left[\frac{\lambda}{\pi D} - \frac{1}{p\cos\alpha}\right]\right\}.$$

Nakano, in Fig. 3, presents his data for the angle $\theta = 180^\circ - \phi$. Accordingly, the expression for θ incorporates a negative sign

$$\theta = \arccos\left\{\frac{-1}{\tan\alpha}\left[\frac{\lambda}{\pi D} - \frac{1}{p\cos\alpha}\right]\right\}.$$

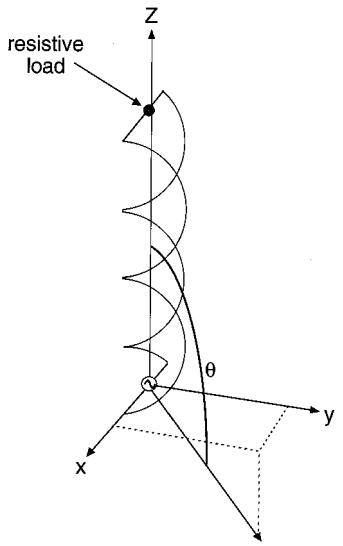

Fig. 1. Nakano *et al.* [1] used a six-turn resistively terminated bifilar helix in their numerical experiment to emulate the performance of a longer helix.

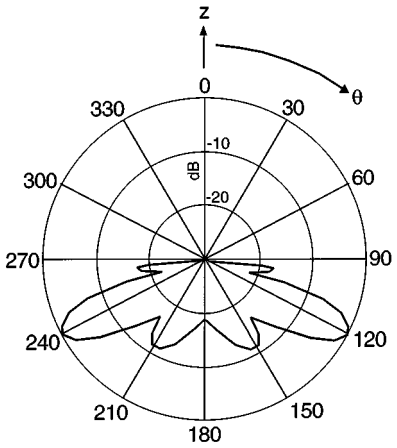

Fig. 2. Major backfire conical lobe documented by Nakano *et al.* in [1].

III. Results

Nakano *et al.* [1] used the following values in their paper:

$$\alpha = 68^\circ$$
$$D = 1.6 \text{ cm}$$
$$\lambda = 23 \text{ to } 12 \text{ cm} \quad (\text{Frequency} = 1.3 \text{ to } 2.5 \text{ GHz}).$$

Using these values with the above equation for θ, we may plot the direction of the major radiation lobe versus frequency as in Fig. 6 for the values $p = 0.6 - 1.0$. We see that $p = 1.0$ reproduces the scan data of Nakano (Fig. 3) exactly.

IV. Discussion

The bifilar helical antenna of Nakano operates strictly as a radiating "twisted" parallel transmission line. The relative phase velocity is $p = 1$, as would be expected for a transmission line without dielectric loading. This stands at contrast to the monofilament helical antenna (axial mode) of Kraus [2], which shows a phase velocity between 0.7 and 0.9, self adjusting so as to maintain a maximum endfire condition.

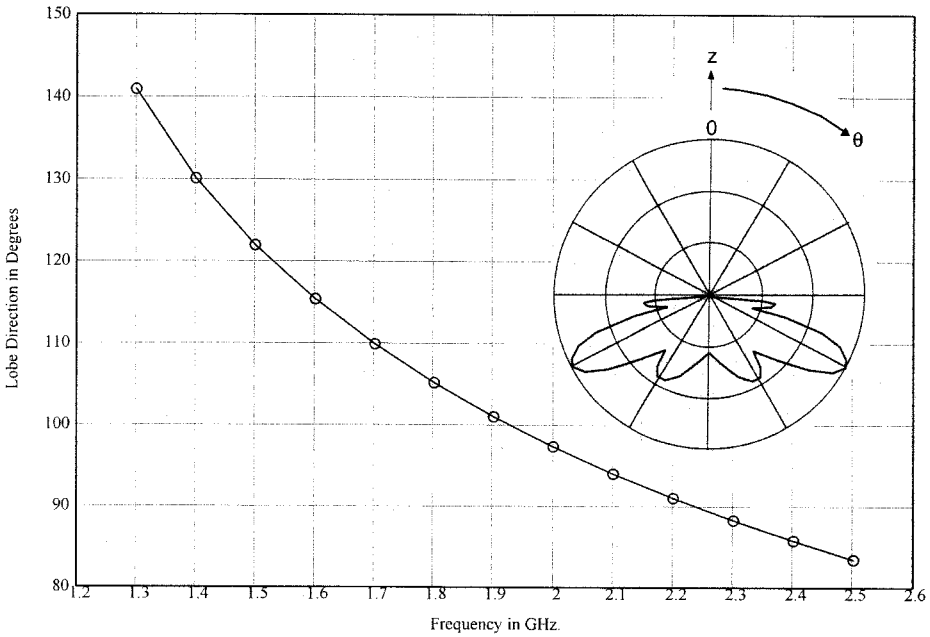

Fig. 3. The conical radiation lobe of Nakano *et al.* [1] scanned from a backfire lobe at 1.3 GHz to a normal lobe at 2.3 GHz.

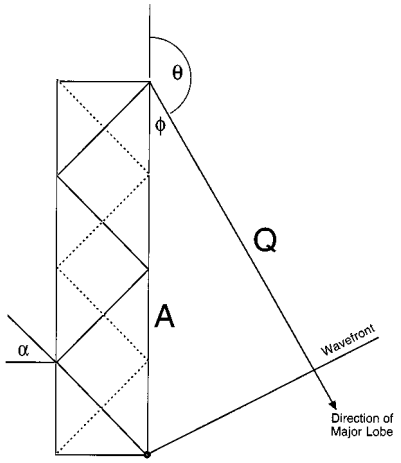

Fig. 4. Crossview of representative helix radiating in direction ϕ. Nakano *et al.* [1] used the angle $\theta = 180^\circ - \phi$.

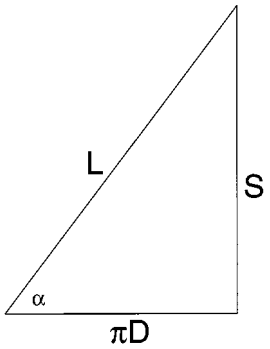

Fig. 5. One turn of the helix unwound to display the relation between the sides and the pitch angle α.

The bifilar helix described here has no phase adjusting mechanism such as this.

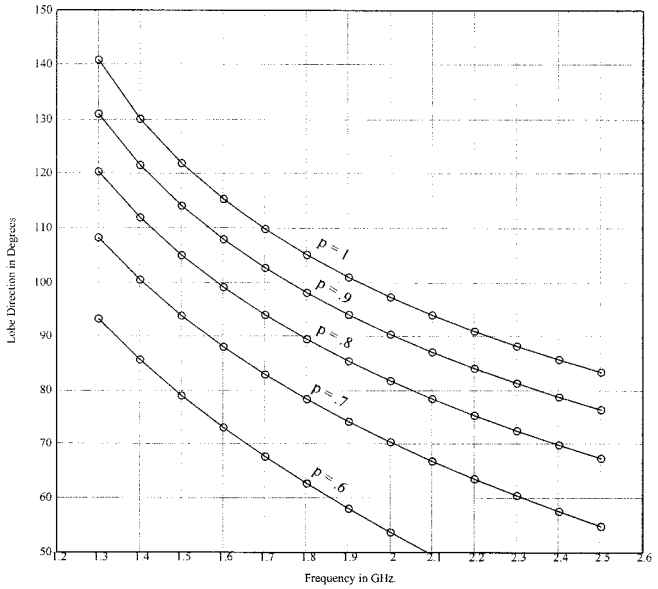

Fig. 6. Calculated lobe direction θ versus frequency in gigahertz for values of $p = v/c$ between 0.6 and 1.0. $p = 1.0$ duplicates Nakano's experimental findings in Fig. 3.

ACKNOWLEDGMENT

The author would like to thank the National Astronomy and Ionosphere Center (N.A.I.C.), Arecibo Observatory, for making time and facilities available to pursue this work. Cornell University operates N.A.I.C. under a cooperative agreement with the National Science Foundation.

REFERENCES

[1] H. Nakano, H. Mimaki, and J. Yamauchi, "Loaded bifilar helical antenna with small radius and large pitch angle," *Electron. Lett.*, vol. 27, no. 17, pp. 1568–1569, 1991.

[2] J. D. Kraus, *Antennas*, 2nd ed. New York: McGraw-Hill, 1988, ch. 7.